

PAPER • OPEN ACCESS

Efficient concentration of trace analyte with ordered hotspot construction for a robust and sensitive SERS platform





To cite this article: Youdi Hu *et al* 2024 *Int. J. Extrem. Manuf.* **6** 035505

View the [article online](#) for updates and enhancements.

You may also like

- [Recent progress in bio-inspired macrostructure array materials with special wettability—from surface engineering to functional applications](#)
Zhongxu Lian, Jianhui Zhou, Wanfei Ren et al.
- [Quantitative Study of Electrochemical Reduction of Ag⁺ to Ag Nanoparticles in Aqueous Solutions by a Plasma Cathode](#)
S. Ghosh, R. Hawtof, P. Rumbach et al.
- [Finding of a Population of Active Galactic Nuclei Showing a Significant Luminosity Decline in the Past 10³–10⁴ yr](#)
Janek Pflugradt, Kohei Ichikawa, Masayuki Akiyama et al.

Efficient concentration of trace analyte with ordered hotspot construction for a robust and sensitive SERS platform

Youdi Hu¹, Yanlei Hu^{2,*} , Zhenyu Wang², Jiale Yong² , Wei Xiong³ , Dong Wu² 
and Shixiang Xu^{1,*}

¹ Shenzhen Key Laboratory of Micro-Nano Photonic Information Technology, College of Physics and Optoelectronic Engineering, Shenzhen University, Shenzhen, Guangdong 518060, People's Republic of China

² CAS Key Laboratory of Mechanical Behavior and Design of Materials, Key Laboratory of Precision Scientific Instrumentation of Anhui Higher Education Institutes, Department of Precision Machinery and Precision Instrumentation, University of Science and Technology of China, Hefei, Anhui 230027, People's Republic of China

³ Wuhan National Laboratory for Optoelectronics, Huazhong University of Science and Technology, Wuhan, Hubei, People's Republic of China

E-mail: huyi@ustc.edu.cn and shxxu@szu.edu.cn

Received 6 July 2023, revised 14 September 2023

Accepted for publication 13 March 2024

Published 4 April 2024



CrossMark

Abstract

Surface-enhanced Raman scattering (SERS) platform, which enables trace analyte detection, has important application prospects. By structuring/modifying the surface of the SERS substrate, analyte in highly diluted solutions can be concentrated into localized active areas for highly sensitive detection. However, subject to the difficulty of the fabrication process, it remains challenging to balance hot-spot construction and the concentration capacity of analyte simultaneously. Therefore, preparing SERS substrates with densely ordered hot spots and efficient concentration capacity is of great significance for highly sensitive detection. Herein, we propose an Ag and fluoroalkyl-modified hierarchical armour substrate (Ag/F-HA), which has a double-layer stacking design to combine analyte concentration with hotspot construction. The microarmour structure is fabricated by femtosecond-laser processing to serve as a superhydrophobic and low-adhesive surface to concentrate analyte, while the anodic aluminium oxide (AAO) template creates a nanopillar array serving as dense and ordered hot spots. Under the synergistic action of hot spots and analyte concentration, Ag/F-HA achieves a detection limit down to 10^{-7} M doxorubicin (DOX) molecules with a RSD of 7.69%. Additionally, Ag/F-HA exhibits excellent robustness to resist external disturbances such as liquid splash or abrasion. Based on our strategy, SERS substrates with directional analyte concentrations are further explored by patterning microcone arrays with defects. This work opens a way to the realistic implementation of SERS in diverse scenarios.

* Authors to whom any correspondence should be addressed.



Original content from this work may be used under the terms of the [Creative Commons Attribution 4.0 licence](https://creativecommons.org/licenses/by/4.0/). Any further distribution of this work must maintain attribution to the author(s) and the title of the work, journal citation and DOI.

Supplementary material for this article is available [online](#)

Keywords: surface-enhanced Raman scattering, anodic aluminium oxide, femtosecond laser processing, concentration of trace analytes, mechanical robustness

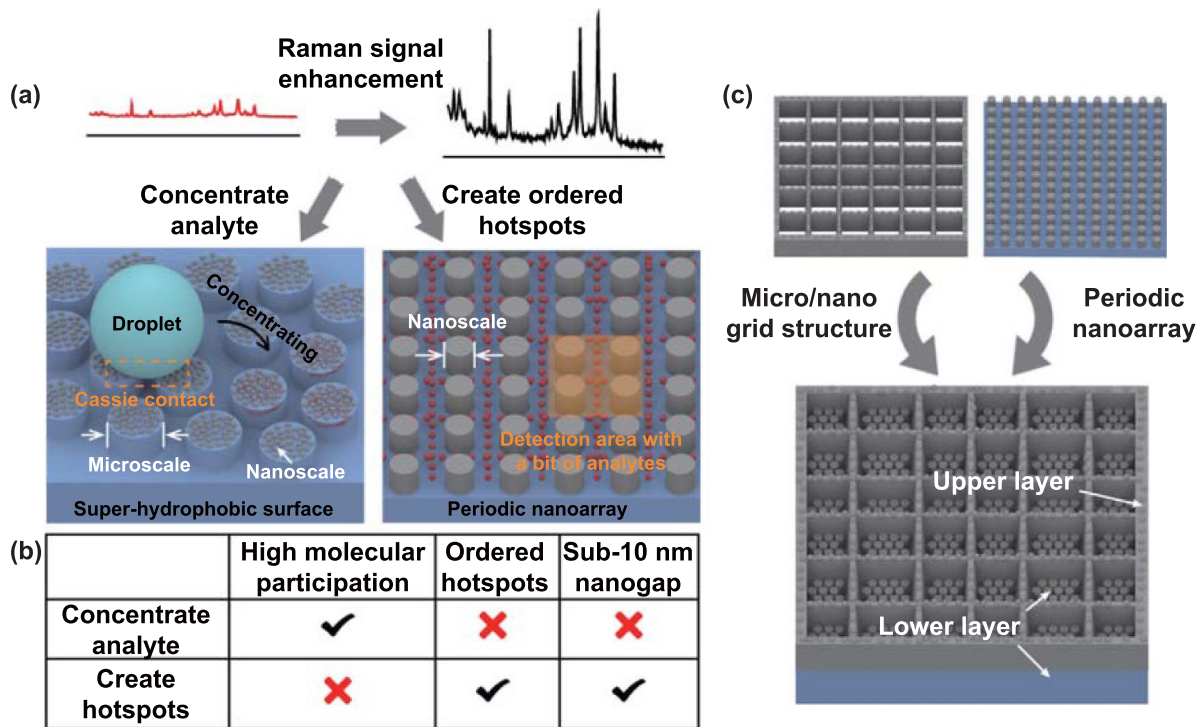
1. Introduction

The detection of analytes in highly diluted solutions is a significant area of research and application, encompassing blood testing [1], food safety [2], and environmental monitoring [3], where high detection sensitivity for weak signals is required. Surface-enhanced Raman scattering (SERS) is an effective method for material characterization, which has been widely employed for molecular detection at low concentrations. By constructing metallic plasmon hotspots [4–6], localized surface plasmon resonance is excited under irradiation to achieve near-electric field enhancement [7]. The conventional approach for signal amplification involves constructing periodic metallic nanoarrays with nanogaps. Subsequently, immersing the SERS substrate in the diluted solution enables analytes to freely diffuse to the hot spot. In this way, the Raman signal is amplified under the action of the near-electric field. However, molecular diffusion consumes a large amount of time, which is not suitable for practical applications [8]. In addition, limited by the spot size of the excitation laser, the effective detection area only occupies a small portion of the entire SERS substrate, which means that only a few molecules contribute to the signals [9]. Consequently, concentrating analytes in the diluted solution into the localized area is developed to achieve highly sensitive detection [10]. However, this method suffers from the coffee-ring effect caused by the adhesion between the droplet and substrate, which forms a fixed contact line. The analytes are driven at the line in the process of liquid evaporation and prevented from localized concentration. Therefore, constructing SERS substrates with specific wettability is of great importance.

Recently, SERS substrates with special surface properties, such as slippery surfaces [8, 11], superhydrophobic surfaces [12, 13], and low-adhesion surfaces [14, 15], have been developed for detection of trace analyte. These special surfaces can overcome the coffee-ring effect and aid in surpassing the diffusion limit and concentrating the analyte within a localized area. However, the slippery surface works in the presence of lubricant, thus inevitably resulting in an impure signal [9]. Superhydrophobic/low-adhesion surfaces have been proven to have the ability to concentrate trace analytes into the localized area. Recently, some works have directly modified nanostructures with low surface energy substances, but it is difficult to achieve both high hydrophobicity and low adhesion properties due to the small surface roughness [16–18]. According to the Cassie contact model [19–21], the micro/nano hierarchical structure can trap more air at the interface to achieve superhydrophobicity and low adhesion. Consequently, various substrates with composite structures have been fabricated and obtained some success in

SERS performance [22, 23]. In these substrates, the nanostructure plays two roles: one is to increase roughness for hydrophobicity, and the other is to provide plasmonic hotspots. However, limited by the processing difficulty of micro/nano hierarchical structures, these plasmonic hot spots are usually disordered and size-uncontrolled, especially when attempting to create the nanogap with sub-10 nm, which is considered to be capable of the strongest near-field enhancement [24]. Scheme 1(a) shows the two routes mentioned above with different structural designs for SERS performance. Obviously, the rational structural design to combine the merits of the two approaches is crucial to signal amplification, which is summarized in scheme 1(b). Additionally, high mechanical stability is also needed for the transference and preservation of the SERS substrate.

Herein, we propose an Ag and fluoroalkyl-modified hierarchical armour (HA) substrate (Ag/F-HA), which has a double-layer stacking design to achieve a synergic effect, as shown in scheme 1(c). The grid structure as an upper layer serves for analyte concentration, while the periodic nanoarray as a lower layer provides dense and ordered hotspots. The preparation of Ag/F-HA involves two steps: the fabrication of the HA substrate and the modification of Ag/F coatings. The HA substrate is fabricated by femtosecond laser processing on an anodized aluminium oxide (AAO) template, and composed of nanoscale pillar arrays and microscale armour structures, where the nanopillar arrays are embedded in each unit cell of the microgrid armour structures. The modification of Ag/F coatings increases the surface roughness of the microarmour structure while reducing the surface energy, which endows Ag/F-HA with superhydrophobic and low-adhesive properties to realize localized concentration. The existence of nanopillars provides the deposition site of Ag to form dense and ordered hotspots with sub-10 nm gaps, which stimulates the strong coupling of localized plasmonic resonance. Ag/F-HA has been applied to the drug detection of doxorubicin (DOX) and exhibits excellent detection capability with a detection limit of 10^{-7} M. Additionally, Ag/F-HA has excellent mechanical robustness to protect the inner nanoarrays from destruction. Based on our strategy, we further explore diverse SERS substrates with microscale structures, which perform the directed concentration of analytes to enable rapid location and detection. Although SERS studies based on fs laser processing have been widely reported [25–27], and most of them have achieved highly sensitive and directional detection, this work exhibits different characteristics, which are summarized in table S1. Our strategy provides a feasible route to fabricate highly sensitive and functional SERS substrates and has broad application prospects for trace analyte detection in various fields.



Scheme 1. Theory of double-layer stacking design. (a) Schematic illustration of two main routes of structure design to Raman signal enhancement. (b) Summary of advantages and disadvantages of concentrating analytes and creating hotspots. (c) A double-layer stacking design to combine the merits of two routes.

2. Results and discussion

2.1. The fabrication and characteristics of a HA substrate

Figure 1(a) shows a schematic diagram of the fabrication process of the HA substrate. The AAO template has a thickness of 125 nm, a pore diameter of 70 nm and a pitch of 100 nm, as shown in figure S1. First, the femtosecond laser is adopted to process the 2D grid pattern on the AAO template to form a linear microgroove array by the line-scanning method [28–30]. Then, poly(methyl methacrylate) (PMMA) solution, prepared by dissolving the PMMA powder into toluene, is drop-coated onto the surface of the grooved template. Subsequently, PMMA film is acquired by natural solvent evaporation. The HA substrate is obtained by removing the back aluminium and the porous alumina layer. Due to the prominent flow property of the PMMA solution, the shapes of the nanochannel and microgroove are inverted conformally as the nanopillar and microwall, respectively. Microwalls pose the interlaced arrangement to form a microarmour structure, and the nanopillar array is located in the interwoven region.

The scanning electron microscopy (SEM) image of the HA substrate is shown in figure 1(b). The x - and y -axis microwalls are aligned perpendicular to each other to form the microarmour structure. The spacing between two adjacent microwalls is 100 μm , as determined by the line distance of laser scanning. This indicates that PMMA inverts the shape of the microgrooves well. Figure 1(c) shows the SEM image for a single cell with an armour structure, where the nanopillar array is distributed in the centre area of 70 $\mu\text{m} \times 70 \mu\text{m}$.

As shown in figure 1(e), each nanopillar has a diameter of 70 nm, and a 30 nm wide nanogap exists between adjacent nanopillars. The nanopillar array has a hexagonal arrangement, and the ordering of the nanopillar array is further verified by the small-angle x-ray scattering (SAXS) technique, as given in figure 1(f), which exhibits the characteristic feature of a hexagonal structure. Figure 1(d) shows the SEM image of a single microwall. Micropillars appear with a pitch of approximately 20 μm on the top of the microwall. This could result from microhole formation in femtosecond laser processing [31, 32]. Interestingly, the existence of micropillars is advantageous for the hydrophobic performance of the HA substrate due to increasing the surface roughness. In addition to the HA substrate with a 100 μm width spacing, substrates with spacings of 200 μm and 400 μm were also fabricated, as shown in figure S2.

2.2. Optimization of processing parameters for HA substrate

The hydrophobic property of the HA substrate is strongly dependent on the morphology of the HA substrate, which is directly determined by the ablated AAO template. Three key parameters (height, width, and jetting length) related to the morphology of the laser-ablated AAO template are studied, as shown in the schematic in figure 2(a). Note that the ablation process could produce a high-heat liquid jet, and the cooling product was redeposited onto the surface of the AAO template. It is regarded as a contaminant that blocks nanochannels and harms the following inversion process. As a result,

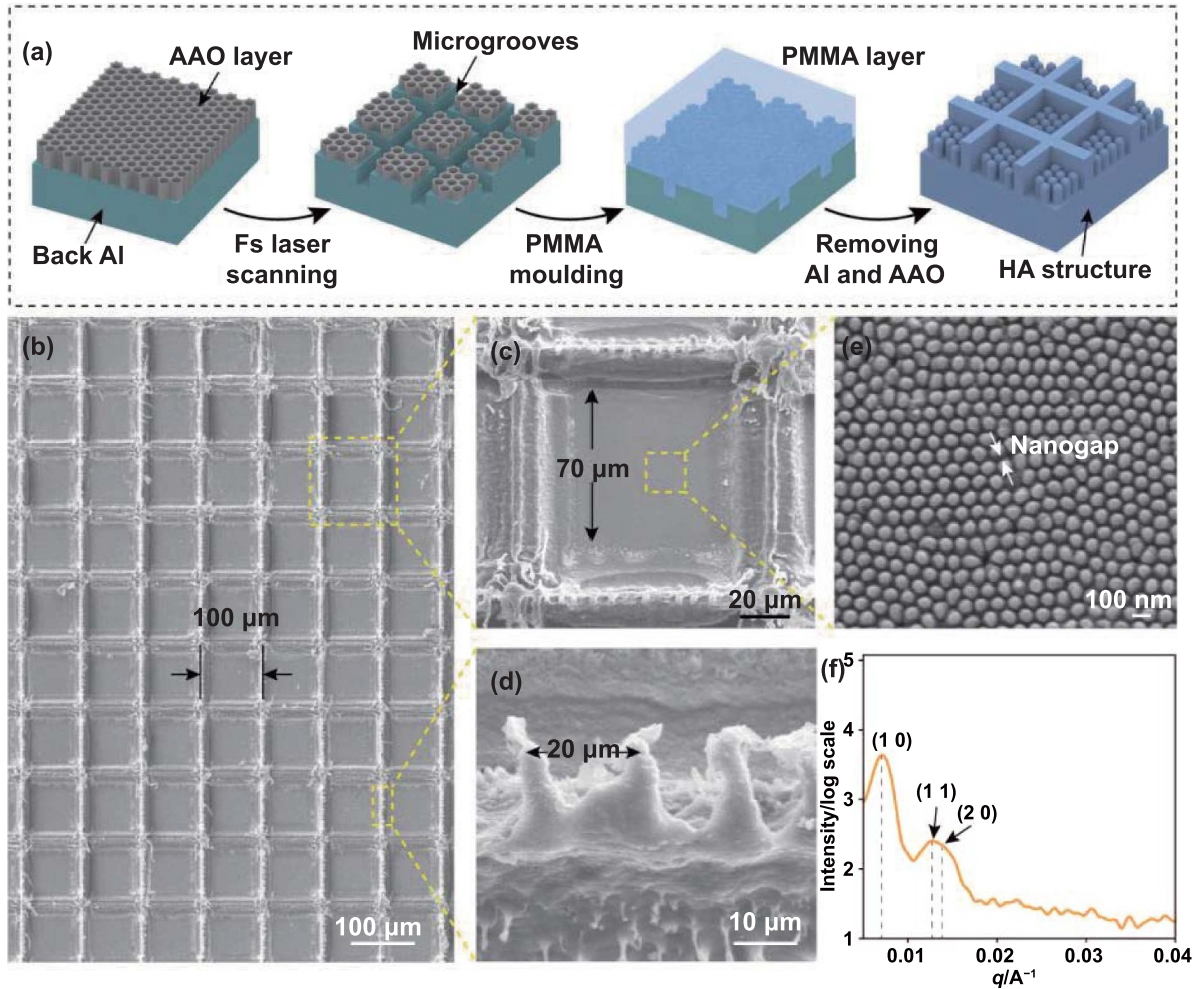


Figure 1. Preparation and characterization of HA substrate. (a) Schematic flow diagram of the fabrication process. (b) SEM image of the HA substrate with a 7×10 unit cell array. (c) SEM image of a unit cell in (b). (d) SEM image of the microwall in (b). (e) Magnified SEM image of the selected yellow area in (c). (f) SAXS measurement of the HA substrate.

we explore the impact of the laser power on the jetting distance. As shown in figure 2(b), when the laser power decreases from 200 mW to 100 mW, the jetting distance shortens from $69 \mu\text{m}$ to $20 \mu\text{m}$. The insets of optical images also exhibit the reduced area covered by sediment as the laser power decreases. When the laser power decreases to 50 mW, a clean surface is obtained without sediment deposition. In addition, the impact of scanning cycles and laser power on groove morphology is discussed. In figure 2(c), the groove width and height increase rapidly within 50 cycles and finally stabilize. Different from scanning cycles, the lifting power results in the groove height increasing linearly, as shown in figure 2(d). These results indicate that both the scanning cycle and laser power are two significant factors that control the groove morphology.

2.3. The wettability of the Ag/F-HA substrate

It is essential to decrease the surface energy and increase the roughness to realize superhydrophobic surfaces with low adhesion. Therefore, a two-step process is implemented: evaporating a 20 nm thick Ag film onto the HA substrate and modifying it with a fluoro-alkyl silane (FAS) layer subsequently, as

illustrated in figure 3(a). Here, the HA substrate with the Ag coating is named 'Ag-HA', and the HA substrate with both the Ag coating and FAS modification is named 'Ag/F-HA'. Notably, Ag film has two important roles. The part deposited into the nanogap between adjacent nanopillars can excite coupling of localized plasma resonance and achieve Raman signal enhancement. Figure S3 shows SEM images of the nanopillar array with deposited Ag. Hotspots with a sub-10 nm gap appear and have a hexagonal and uniform distribution. Moreover, a thin Ag film can increase the microwall surface roughness and reduce the surface energy, which changes the liquid-substrate wettability model from a Wenzel contact to a transition contact. After FAS modification, low surface energy contributes to more gas capture between the droplet and substrate to realize Cassie contact. Figure 3(b) shows the contact angle measurements on the different substrates. By changing the line distance of laser scanning, HA substrates with unit cell side lengths of $100 \mu\text{m}$, $200 \mu\text{m}$, and $400 \mu\text{m}$ can be obtained, denoted as HA-100, HA-200, and HA-400, respectively. The substrate fabricated by a conventional AAO template without laser processing is denoted as a nanoarray film. The nanoarray film without coating has a contact angle

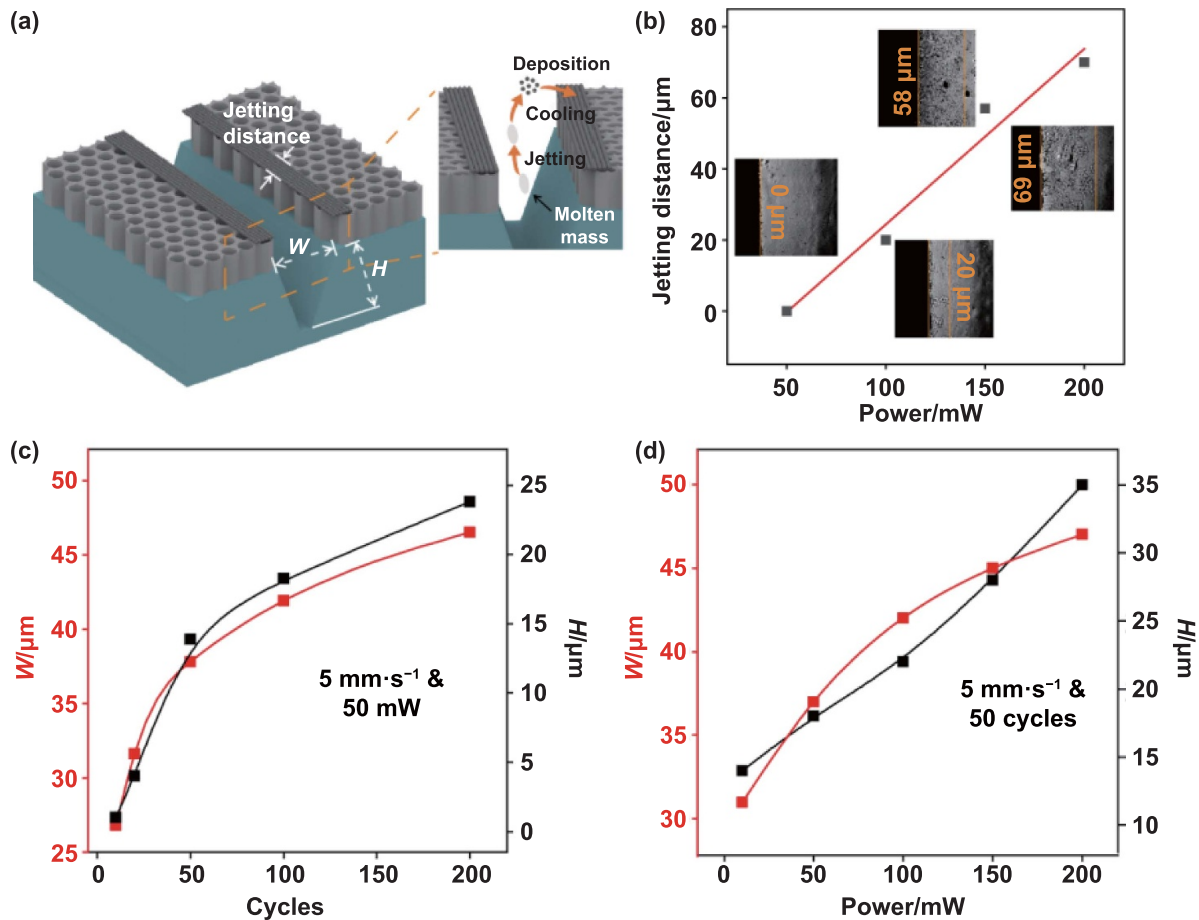


Figure 2. Effect of the process parameters on the morphology. (a) Schematic diagram of the structural parameter and laser-induced jetting. (b) Jetting distance of ablation-created sediment under different laser powers. The insets show optical images of grooves after laser ablation. (c)–(d) The width and height of the ablated groove on the AAO template surface under different scanning cycles (c) and laser powers (d).

of 95° . The natural hydrophobicity of PMMA indicates that the nanopillar structure contributes little to the hydrophobic performance. When evaporating the Ag coating, the contact angle increases to 120° , which is attributed to the reduced surface energy and enhanced surface roughness. By modifying FAS subsequently, the hydrophobic performance slightly improved as the contact angle increased from 120° to 125° , and the limited improvement in hydrophobicity might be due to the absence of microstructure. We therefore investigated the effect of the microarmour structure on substrate hydrophobicity. As shown in figure 3(b), the HA substrates appear to have a similar rising trend to the nanoarray film in terms of hydrophobicity. For the HA substrate with the same coating, the smaller the line distance is, the more hydrophobic the substrate is. As the line distance decreases to $100 \mu\text{m}$, both Ag-HA-100 and Ag/F-HA-100 exhibit superhydrophobic properties. In addition to hydrophobicity, adhesion is also an important factor in substrate surface properties, which facilitates droplet concentration and prevents the coffee-ring effect. Therefore, the slide angle measurement was carried out on both Ag-HA and Ag/F-HA substrates to evaluate the adhesion performance. As shown in figure 3(c), for the Ag-HA substrate, the droplets exhibit slide angles of 20.8° , 70.1° , and 180° on Ag-HA-100, Ag-HA-200, and

Ag-HA-400, respectively. It appears that a broad line distance results in a large slide angle, which is caused by the high adhesion between the droplet and substrate, and forms a fixed contact line. After FAS modification, the slide angles dramatically decrease to 4.5° , 7.5° and 18° , corresponding to Ag/F-HA-100, Ag/F-HA-200, and Ag/F-HA-400, respectively. This indicates that the improved sliding performance of the Ag/F-HA substrate is due to the chemical modification of the low surface energy, which effectively decreases the surface adhesion.

2.4. Measurement and investigation of the SERS performance of the Ag/F-HA substrate

Figure 4(a) shows the *ex-situ* contact angle measurement to observe the evaporation process of a $5 \mu\text{l}$ rhodamine 6G (R6G) droplet with a concentration of 10^{-7} M , which is located on the surface of the Ag/F-HA-100 or nanoarray film. For Ag/F-HA-100 (the pink region of figure 4(a), movie S1), the droplet shrinks in volume during evaporation and maintains a quasi-spherical shape in 39 min. This results from the low adhesion force, which avoids the contact line being pinned at the initial position. Therefore, the R6G molecules are concentrated in a confined area (the pink box of figure 4(a)). In comparison, the

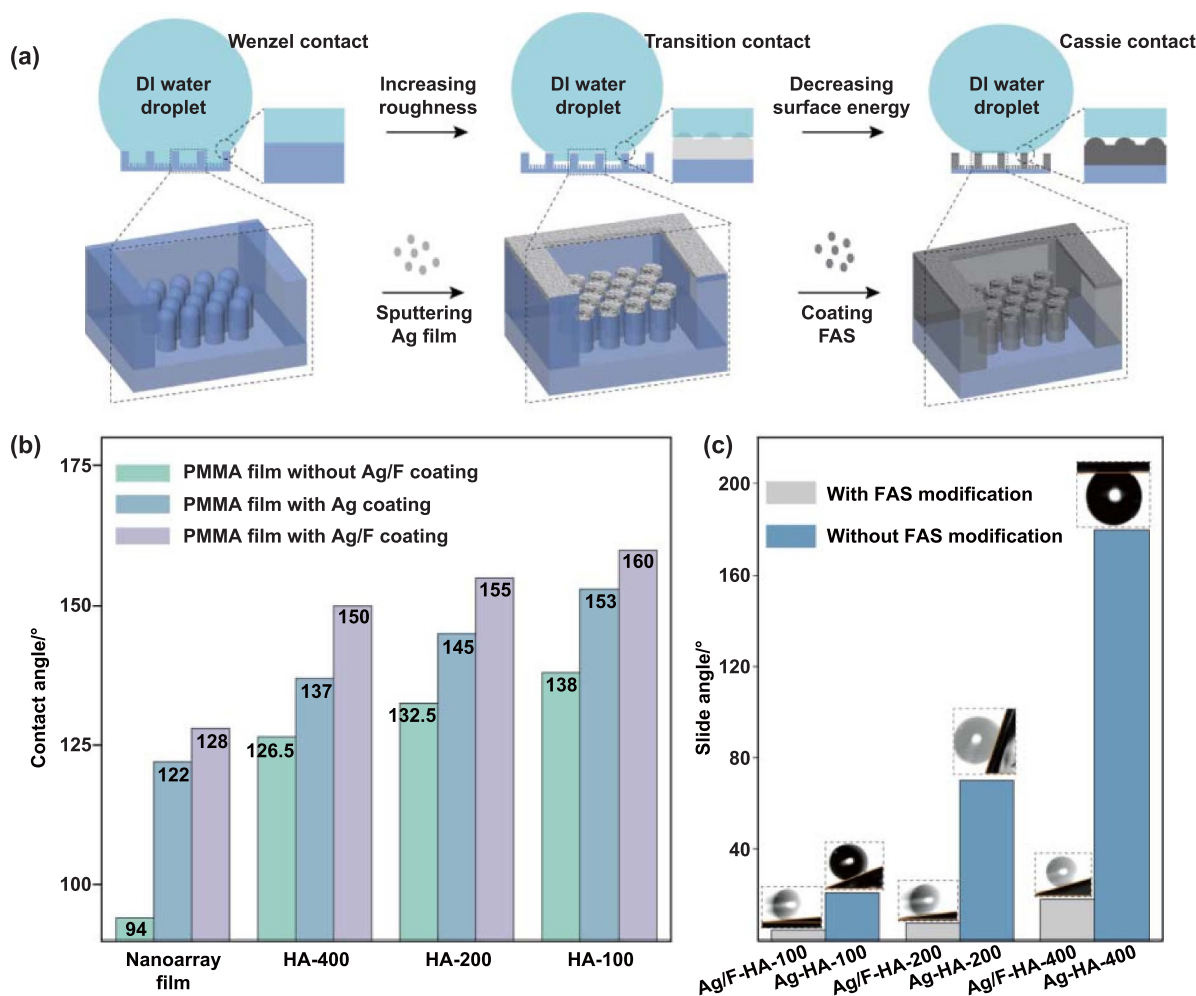


Figure 3. Wettability characterization of Ag/F-HA substrate. (a) Schematic diagram of the fabrication process of the Ag/F-HA substrate and the contact model between the droplet and surface at the different processing stages. (b) Contact angle measurements for the nanoarray film, HA-100, HA-200, and HA-400. (c) Slide angle measurements with and without FAS modification for Ag-HA-100, Ag-HA-200, and Ag-HA-400.

initial contact angle (CA) is only 120° for the nanoarray film with Ag and FAS coatings (the yellow region of figure 4(a), movie S2). Affected by high adhesion, the CA obviously decreases with time, and the contact line is almost pinned on the surface with a slight drawback. The target molecules diffuse to the contact line due to the effect of capillary force and eventually deposit at the contact line to form a coffee ring (the yellow box of figure 4(a)). The optical images of the deposition area for Ag/F-HA-200 and Ag/F-HA-400 are also shown in figure S4. The size of the deposition area on the four different substrates is computed in figure 4(b). The nanoarray film has the largest deposition area of almost 1.13 mm^2 , caused by the coffee ring effect. For Ag/F-HA, there are deposition areas of 0.06 mm^2 , 0.08 mm^2 and 0.16 mm^2 on Ag/F-HA-100, Ag/F-HA-200, and Ag/F-HA-400, respectively. The narrower the line distance is, the smaller the deposition area is. Moreover, the concentration factor of Ag/F-HA-100 is evaluated [33], and the result reaches approximately 84, which shows that the substrate exhibits good performance for the analyte concentration. We further collect the Raman spectra on four different substrates, which are measured after evaporating a $5 \mu\text{l}$

R6G droplet with a concentration of 10^{-7} M . As shown in figure 4(c), one can find that there is a very weak detectable signal on the nanoarray film, while all three Ag/F-HAs give strong Raman spectra. Note that the Raman intensity of Ag/F-HA-100 is approximately 30 times stronger than that of the nanoarray film. Meanwhile, the deposition area for Ag/F-HA-100 has an almost 20-fold drop compared to that for the nanoarray film, as shown in figure 4(b). This reveals that the degree of concentration determines the intensity of the Raman signal. The reproducibility of SERS measurements is another important factor. To further explore the effect of scanning spacing on Raman signals, we reduced the line distance to $70 \mu\text{m}$, and the prepared substrate was named Ag/F-HA-70. Figure S5 shows SEM images of Ag/F-HA-70 at different magnifications. Obviously, when the line spacing is reduced to $70 \mu\text{m}$, the coverage area of the nanopillar array is only $20 \mu\text{m} \times 10 \mu\text{m}$ due to the fixed size of the laser focus spot. In other words, the area occupied by high-density ordered hotspots is very small. The Raman spectrum is measured by concentrating a $5 \mu\text{l}$ R6G droplet with 10^{-7} M , as shown in figure S6. By comparison of the Raman spectra, the intensity

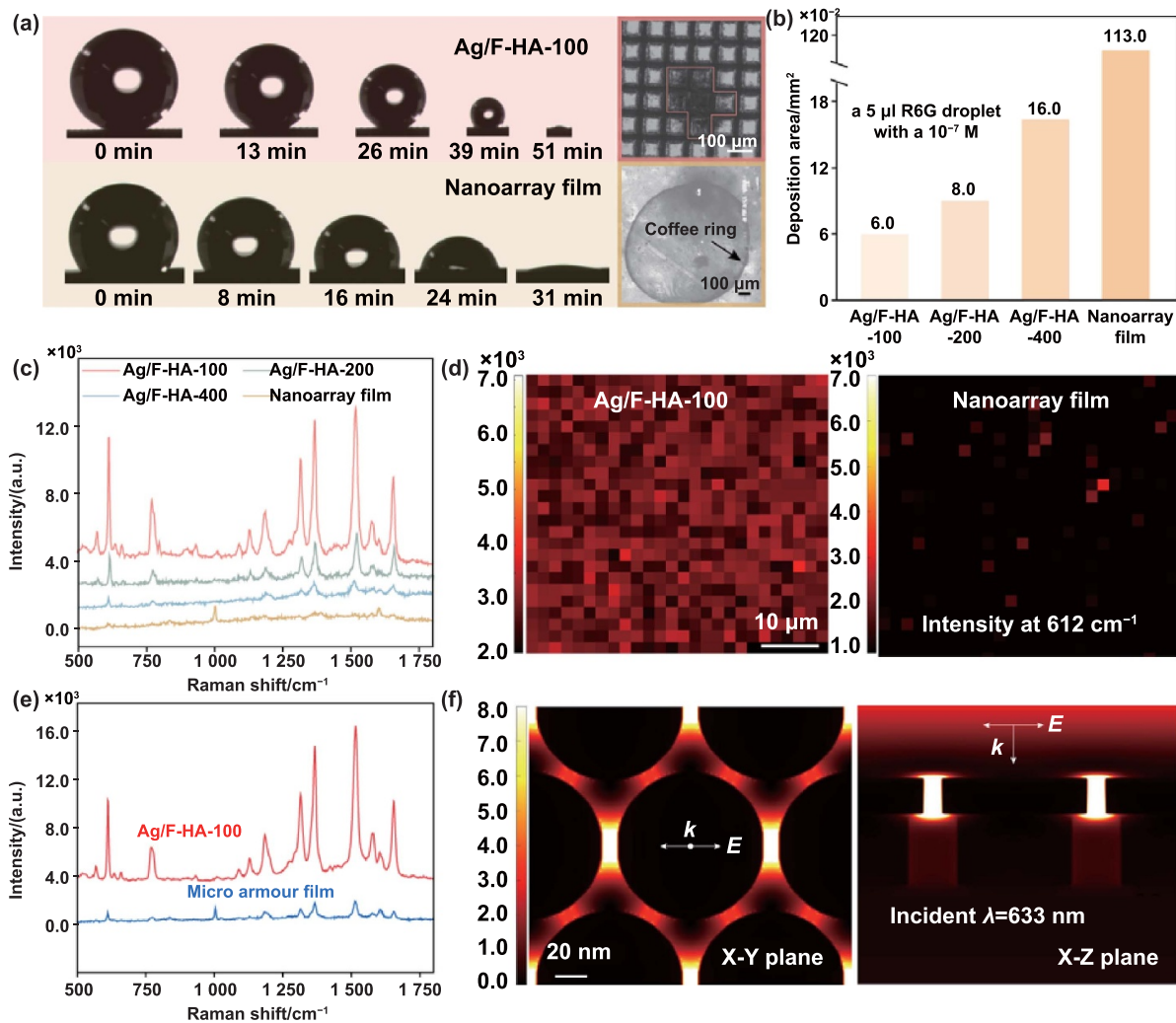


Figure 4. Raman characterization of the Ag/F-HA substrate. (a) *Ex situ* contact angle measurement during droplet evaporation at five different times and optical images of the deposition conditions for R6G molecules on Ag/F-HA-100 and the nanoarray film. (b) The deposition area of a 5 μl R6G droplet with a concentration of 10^{-7} M after evaporation on the nanopillar film, Ag/F-HA-100, Ag/F-HA-200, and Ag/F-HA-400. (c) Raman spectra of R6G molecules under the condition of (b). (d) Raman intensity mapping at a distinct peak of 612 cm^{-1} for Ag/F-HA-100 and the nanoarray film. (e) Comparison of Raman spectra of Ag/F-HA-100 and the microarmour film. (f) The FDTD simulation for the nanopillar array at normal incident.

of Ag/F-HA-70 is smaller than that of Ag/F-HA-100, which could result from the insufficient deposition of R6G to the small area of the nanoarray. To demonstrate that Ag/F-HA has a high homogeneity, Raman mapping of the R6G molecule is implemented. Figure 4(d) shows the intensity distribution of the characteristic peak at 612 cm^{-1} obtained from 625 sample points within a collected area of $50\ \mu\text{m} \times 50\ \mu\text{m}$. Ag/F-HA-100 exhibits strong and uniform Raman signals, with a relative standard deviation (RSD) of 13.7%. In comparison, the SERS signals from the nanoarray film show a weak and uneven distribution.

In addition to hydrophobicity, the hotspot also has a significant impact on SERS performance. To control the experiments, a microarmour structure without an inner nanopillar array is fabricated by replacing the AAO template with polished aluminium, and the obtained substrate is named 'microarmour film'. The Raman spectra are collected after evaporating the target droplets, as shown in figure 4(e). It

is obvious that all characteristic peaks are detected for the microarmour film, which reflects the effect of hydrophobicity on SERS performance. However, Ag/F-HA-100 exhibits a Raman signal 10 times stronger than that of the microarmour film. This reveals that nanoscale hot spots contribute mainly to the enhanced intensity. The SERS phenomenon is explained by finite-difference time domain (FDTD) simulations. The distribution of the electric field intensity ($|E/E_0|^2$) of the nanopillar array is shown in figure 4(f) with normalized illumination under $\lambda = 633\text{ nm}$. Obvious electric enhancement can be observed between Ag nanoparticles located on the adjacent PMMA nanopillars, which is attributed to the intensive coupling of localized surface plasmons between adjacent Ag nanoparticles. Moreover, we also researched the effect of FAS modification on SERS performance. As shown in figure S7, Ag/F-HA-100 shows a stronger SERS intensity than Ag-HA-100, which indicates that the low adhesion surface has a positive effect on the Raman spectrum. To

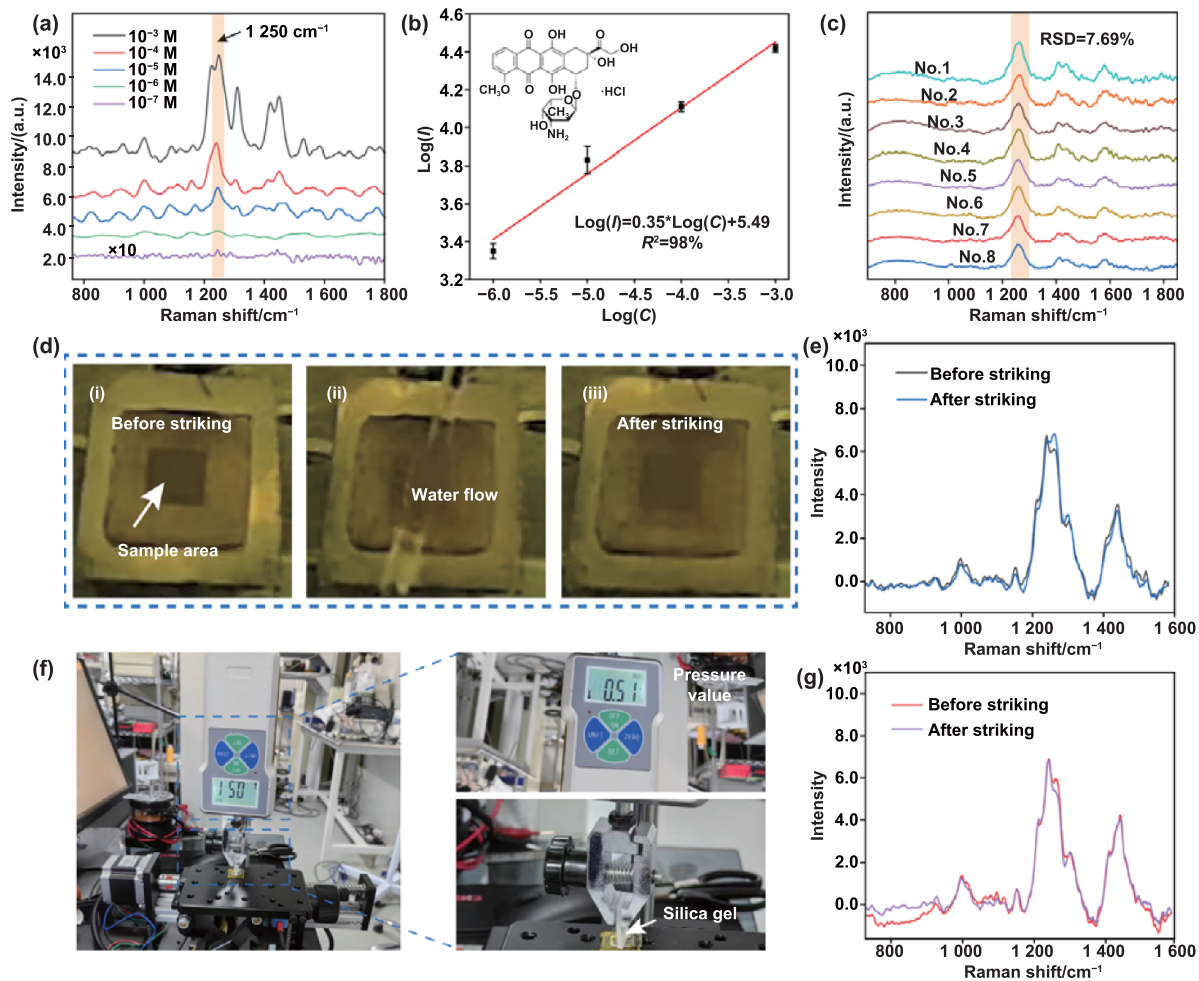


Figure 5. Detection of DOX molecules. (a) Raman spectra collected from a DOX droplet of $3 \mu\text{l}$ with a concentration range from 10^{-3} to 10^{-7} M. (b) $\text{Log}(I)$ - $\text{log}(C)$ plot of SERS intensity at 1250 cm^{-1} . (c) Uniformity measurement of Raman spectra from eight random points. (d) Optical images indicating the flow striking substrate surface. (e) Raman spectra of DOX before and after striking. (f) Optical image of lab-made abrasion equipment with an applied pressure of 0.5 N to the substrate. (g) Raman spectra of DOX before and after abrasion.

further evaluate the detection limit of Ag/F-HA-100, Raman spectra collected from R6G droplets with concentrations ranging from 10^{-9} to 10^{-12} M are displayed in figure S8. Even when the concentration is down to 10^{-12} M, the main Raman peaks can still be detected in the spectrum, demonstrating the high detection sensitivity of Ag/F-HA-100. The enhancement factor (EF) of Ag/F-HA-100 prepared in the detection of R6G molecules is estimated to be 0.7×10^9 . Additionally, the effect of nanogap size on SERS performance is studied. By controlling the Ag film thickness to 30 nm, 70 nm, and 140 nm, Ag/F-HA-100s with gap sizes of 20 nm, 6 nm, and 0 nm were prepared, as shown in figure S9. Figure S10 shows the Raman spectra of three substrates with different thicknesses. Obviously, the sample with a 0 nm gap exhibits the weakest signal, indicating that the presence of a nanogap is crucial for enhancing SERS performance. Meanwhile, the signal from the sample with a 20 nm gap is smaller than that with a 6 nm gap, which suggests that a smaller nanogap can lead to stronger signal enhancement. Finally, inspired by the protection of ‘armour’, it is deduced that the microarmour structure has excellent mechanical robustness

to protect the inner nanoarrays from destruction. Therefore, the surface of Ag/F-HA-100 is exposed to repeated abrasion, which is performed by using rubber gloves, as shown in figure S11. The signal intensity has little drop after 100 abrasion cycles, which is attributed to the excellent structure.

Doxorubicin (DOX) is a DNA intercalating agent that is used in anticancer therapy. However, due to the toxicity of cardiac and hematopoietic cells, accurate detection of the DOX concentration plays a vital role in the therapeutic effect [34]. To evaluate the detection limit, Raman spectra collected from DOX droplets with concentrations ranging from 10^{-3} to 10^{-7} M are shown in figure 5(a). Even when the concentration is down to 10^{-7} M, the main Raman peak at 1250 cm^{-1} can still be detected, which is assigned to ring stretching. Figure 5(b) illustrates a $\text{log}(I)$ - $\text{log}(C)$ plot of SERS intensity at 1250 cm^{-1} , which establishes a linear relationship with the increasing concentration of DOX. To verify the uniformity, Raman spectra from eight random points are collected in figure 5(c). As seen, Ag/F-HA-100 exhibits uniform Raman signals, with a RSD of 7.69% at the characteristic

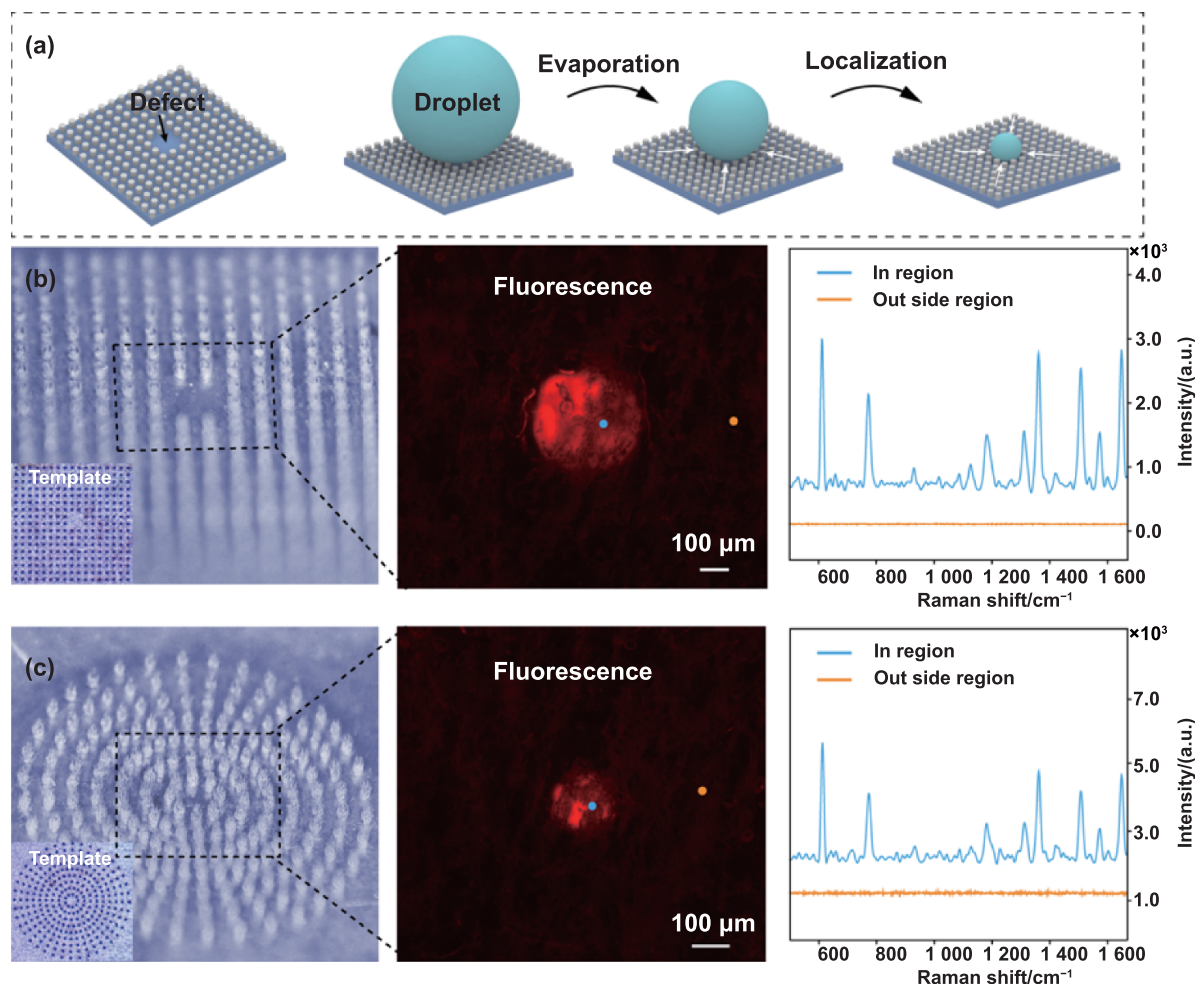


Figure 6. Directional concentration and detection of the PMMA microcone array. (a) Schematic diagram of droplet evaporation and localization on the PMMA microcone array with a spatial defect. (b) and (c) Optical and fluorescence images of microcone arrays with tetragonal and radial arrangements, respectively. The first column shows the optical image of the microcone array by inverting, and the insert shows the optical image of the AAO template with hole arrays by femtosecond laser ablation. The second column shows the fluorescence image of the microcone array after the R6G droplet evaporates and localizes. The third column shows the Raman spectra in and outside the defect region.

peak of 1250 cm^{-1} . Additionally, we simulate the scenario of contamination of prepared samples that may occur during detection, such as liquid splash or abrasion with a solid surface. Figure 5(d) shows the dynamic process with water flow striking the substrate surface. Benefitting from the superhydrophobicity, the surface has no water stains, and liquids cannot penetrate and destroy the hotspots at the bottom. Figure 5(e) shows the spectrum comparison before and after striking, and little attenuation of the signals shows excellent resistance to liquid penetration. Anti-abrasion performance is also characterized by lab-made abrasion equipment, and the probe is made of silica gel, as shown in figure 5(f). Under the action of 0.5 N pressure, the silica-gel probe rubs against the substrate surface. As shown in figure 5(g), abrasion cannot negatively affect Raman signals, which demonstrates mechanical stability. Figure S12 shows optical images before and after abrasion. As we can see, the surface structure remains intact, which further explains the anti-abrasion performance.

To demonstrate the feasibility of our strategy, we further explored diverse SERS substrates with special micron

structures, rather than microarmor structures, to achieve directional concentration performance [35]. As shown in the schematic in figure 6(a), by constructing a spatial defect at the centre of an array, the droplet evaporates and localizes at a special point due to hydrophobic radial forces. To investigate the impact of defects, we fabricated PMMA microcone arrays with and without defects (as schematically shown in figures S13(a) and (d)). Figures S13(b) and (e) show the static contact angle measurements. The droplet localized on the defect site exhibits a spherical contact line, indicating that the droplet penetrates into the defect. In contrast, the droplet on the substrate without the defect shows a flat contact line, which indicates that the microcones can support the droplet (typical Cassie state). Figures S13(c) and (f) show the sliding angle measurements (movies S3 and S4). The defect-free substrate exhibits a smaller sliding angle (2°) than the substrate with a defect (8°). This reveals that there is a stronger binding effect between the defect and droplet than that between the microcone and droplet, which results in the directional concentration. Figures 6(b) and (c) show optical images of the PMMA

microcone arrays with tetragonal and radial arrangements. The centre of the array is absent for microcones and is regarded as a spatial defect. The fluorescence images show the spatial distribution of target molecules after evaporating the droplet, as shown in the second column of figures 6(b) and (c). As expected, the fluorescence signal of the R6G molecule is located in the defect region, which confirms that the microcone array with a spatial defect can realize on-demand concentration of the target molecules. The third column of figures 6(b) and (c) shows the Raman spectra collected in and outside the defect region. The signal in the region exhibits a strong intensity, while there is no signal of any characteristic peaks outside the region. This further demonstrates the capability of our strategy in fabricating directionally concentrated SERS substrates.

3. Conclusion

This work provides a novel strategy by combining densely ordered hotspots with excellent concentration capacity to achieve highly sensitive SERS detection. The Ag/F-HA substrate is applied to drug detection of DOX molecules in highly diluted solution and reaches a detection limit of 10^{-7} M. Due to its unique ‘armour’ structure, Ag/F-HA shows robust mechanical stability to prevent external forces from destroying nanoscale hot spots. Benefiting from the flexibility of femtosecond laser processing, SERS substrates with directional analyte concentration have also been fabricated by patterning a microcone array with a defect to realize the rapid location and detection of analytes. This SERS substrate-enabled trace analyte detection has broad application prospects in various fields, including food safety, biological detection, and environmental monitoring.

Acknowledgments

This work was financially supported by National Natural Science Foundation of China (Nos. 92050203, 52122511, 52305319, 52375582); Shenzhen Fundamental Research Program (Nos. JCYJ20200109105606426, JCYJ20190808164007485). The evaporation experiment and SEM characteristic in this work were carried out at the USTC Center for Micro- and Nanoscale Research and Fabrication. Wei Li engineer provided the powerful support for SEM characterization.

Conflict of interest

The authors declare no competing financial interest.

ORCID iDs

Yanlei Hu  <https://orcid.org/0000-0003-1964-0043>
 Jiale Yong  <https://orcid.org/0000-0003-2144-7330>
 Wei Xiong  <https://orcid.org/0000-0002-2532-2503>
 Dong Wu  <https://orcid.org/0000-0003-0623-1515>

References

- [1] Lin X L, Lin D, Chen Y, Lin J C, Weng S Y, Song J B and Feng S Y 2021 High throughput blood analysis based on deep learning algorithm and self-positioning super-hydrophobic SERS platform for non-invasive multi-disease screening *Adv. Funct. Mater.* **31** 2103382
- [2] Wang T J, Barveen N R, Liu Z Y, Chen C H and Chou M H 2021 Transparent, flexible plasmonic Ag NP/PMMA substrates using chemically patterned ferroelectric crystals for detecting pesticides on curved surfaces *ACS Appl. Mater. Interfaces* **13** 34910–22
- [3] Xu J W, Xiao X, Zhang W B, Xu R, Kim S C, Cui Y, Howard T T, Wu E and Cui Y 2020 Air-filtering masks for respiratory protection from PM_{2.5} and pandemic pathogens *One Earth* **3** 574–89
- [4] Shi Q Q, Gómez D E, Dong D S, Sikdar D, Fu R F, Liu Y Y, Zhao Y M, Smilgies D M and Cheng W L 2019 2D freestanding Janus gold nanocrystal superlattices *Adv. Mater.* **31** 1900989
- [5] Yan X N, Chen Q, Song Q, Huo Z Y, Zhang N and Ma M M 2021 Continuous mechanical tuning of plasmonic nanoassemblies for tunable and selective SERS platforms *Nano Res.* **14** 275–84
- [6] Das A, Pant U, Cao C, Moirangthem R S and Kamble H B 2023 Fabrication of plasmonic nanopyrarnidal array as flexible SERS substrate for biosensing application *Nano Res.* **16** 1132–40
- [7] Xu H X and Käll M 2002 Surface-plasmon-enhanced optical forces in silver nanoaggregates *Phys. Rev. Lett.* **89** 246802
- [8] Zhang D J, Peng L Q, Shang X L, Zheng W X, You H J, Xu T, Ma B, Ren B and Fang J X 2020 Buoyant particulate strategy for few-to-single particle-based plasmonic enhanced nanosensors *Nat. Commun.* **11** 2603
- [9] Chen X Y, Ding Q Q, Bi C, Ruan J and Yang S K 2022 Lossless enrichment of trace analytes in levitating droplets for multiphase and multiplex detection *Nat. Commun.* **13** 7807
- [10] De Angelis F *et al* 2011 Breaking the diffusion limit with super-hydrophobic delivery of molecules to plasmonic nanofocusing SERS structures *Nat. Photon.* **5** 682–7
- [11] Tang S Y, Li Y, Huang H, Li P H, Guo Z N, Luo Q, Wang Z, Chu P K, Li J and Yu X F 2017 Efficient enrichment and self-assembly of hybrid nanoparticles into removable and magnetic SERS substrates for sensitive detection of environmental pollutants *ACS Appl. Mater. Interfaces* **9** 7472–80
- [12] Liu Y H, Zhang N, Tua D, Zhu Y K, Rada J, Yang W H, Song H M, Thompson A C, Collins R L and Gan Q Q 2022 Superhydrophobic 3D-assembled metallic nanoparticles for trace chemical enrichment in SERS sensing *Small* **18** 2204234
- [13] Wu Y W, Hang T, Komadina J, Ling H Q and Li M 2014 High-adhesive superhydrophobic 3D nanostructured silver films applied as sensitive, long-lived, reproducible and recyclable SERS substrates *Nanoscale* **6** 9720–6
- [14] Xu K C, Zhang C T, Zhou R, Ji R and Hong M H 2016 Hybrid micro/nano-structure formation by angular laser texturing of Si surface for surface enhanced Raman scattering *Opt. Express* **24** 10352–8
- [15] Yu J, Wu J E, Yang H, Li P, Liu J, Wang M, Pang J H, Li C B, Yang C and Xu K C 2022 Extremely sensitive SERS sensors based on a femtosecond laser-fabricated superhydrophobic/-philic microporous platform *ACS Appl. Mater. Interfaces* **14** 43877–85
- [16] Lee H K, Lee Y H, Zhang Q, Phang I Y, Tan J M R, Cui Y and Ling X Y 2013 Superhydrophobic surface-enhanced Raman scattering platform fabricated by assembly of Ag nanocubes

- for trace molecular sensing *ACS Appl. Mater. Interfaces* **5** 11409–18
- [17] Geng F, Zhao H P, Fu Q, Mi Y, Miao L K, Li W, Dong Y L, Wu M H and Lei Y 2018 Gold nanochestnut arrays as ultra-sensitive SERS substrate for detecting trace pesticide residue *Nanotechnology* **29** 295502
- [18] Zhang H H, Zhou F, Liu M, Liu D L, Men D D, Cai W P, Duan G T and Li Y 2015 Spherical nanoparticle arrays with tunable nanogaps and their hydrophobicity enhanced rapid SERS detection by localized concentration of droplet evaporation *Adv. Mater. Interfaces* **2** 1500031
- [19] Yang Y et al 2021 Femtosecond laser regulated ultrafast growth of mushroom-like architecture for oil repellency and manipulation *Nano Lett.* **21** 9301–9
- [20] Yong J L, Yang Q, Hou X and Chen F 2022 Nature-inspired superwettability achieved by femtosecond lasers *Ultrafast Sci.* **2022** 9895418
- [21] Yong J L, Singh S C, Zhan Z B, Chen F and Guo C L 2019 How to obtain six different superwettabilities on a same microstructured pattern: relationship between various superwettabilities in different solid/liquid/gas systems *Langmuir* **35** 921–7
- [22] Wang A D, Jiang L, Li X W, Xie Q, Li B H, Wang Z, Du K and Lu Y F 2017 Low-adhesive superhydrophobic surface-enhanced Raman spectroscopy substrate fabricated by femtosecond laser ablation for ultratrace molecular detection *J. Mater. Chem. B* **5** 777–84
- [23] Yang H, Gun X Y, Pang G, Zheng Z X, Li C B, Yang C, Wang M and Xu K C 2021 Femtosecond laser patterned superhydrophobic/hydrophobic SERS sensors for rapid positioning ultratrace detection *Opt. Express* **29** 16904–13
- [24] Qu C Y, Guo Q L, Huang G S and Mei Y F 2021 Local cracking-induced scalable flexible silicon nanogaps for dynamically tunable surface enhanced raman scattering substrates *Adv. Mater. Interfaces* **8** 2100661
- [25] Yu J, Yang H, Wu J G, Wu Y X and Xu K C 2023 Ultrafast laser fabrication of surface-enhanced Raman scattering sensors *Opto-Electron. Eng.* **50** 220333
- [26] Xu K C, Zhou R, Takei K and Hong M H 2019 Toward flexible surface-enhanced Raman scattering (SERS) sensors for point-of-care diagnostics *Adv. Sci.* **6** 1900925
- [27] Xu K C, Yan H P, Tan C F, Lu Y Y, Li Y, Ho G W, Ji R and Hong M H 2018 Hedgehog inspired CuO nanowires/Cu₂O composites for broadband visible-light-driven recyclable surface enhanced Raman scattering *Adv. Opt. Mater.* **6** 1701167
- [28] Nakajima A, Omiya M and Yan J W 2022 Generation of micro/nano hybrid surface structures on copper by femtosecond pulsed laser irradiation *Nanomanuf. Metrol.* **5** 274–82
- [29] Meshram T and Yan J W 2023 Formation of laser-induced periodic surface structures on reaction-bonded silicon carbide by femtosecond pulsed laser irradiation *Nanomanuf. Metrol.* **6** 4
- [30] Zhang Y X, Wu D, Zhang Y C, Bian Y C, Wang C W, Li J W, Chu J R and Hu Y L 2023 Femtosecond laser direct writing of functional stimulus-responsive structures and applications *Int. J. Extrem. Manuf.* **5** 042012
- [31] Yong J L, Yang Q, Chen F, Zhang D S, Bian H, Ou Y, Si J H, Du G Q and Hou X 2013 Stable superhydrophobic surface with hierarchical mesh-porous structure fabricated by a femtosecond laser *Appl. Phys. A* **111** 243–9
- [32] Yong J L, Yang Q, Huo J L, Hou X and Chen F 2022 Underwater gas self-transportation along femtosecond laser-written open superhydrophobic surface microchannels (<100 μm) for bubble/gas manipulation *Int. J. Extrem. Manuf.* **4** 015002
- [33] Pavliuk G et al 2020 Ultrasensitive SERS-based plasmonic sensor with analyte enrichment system produced by direct laser writing *Nanomaterials* **10** 49
- [34] Gautier J, Munnier E, Douziech-Eyrolles L, Paillard A, Dubois P and Chourpa I 2013 SERS spectroscopic approach to study doxorubicin complexes with Fe²⁺ ions and drug release from SPION-based nanocarriers *Analyst* **138** 7354–61
- [35] Zhizhchenko A, Kuchmizhak A, Vitrik O, Kulchin Y and Juodkazis S 2018 On-demand concentration of an analyte on laser-printed polytetrafluoroethylene *Nanoscale* **10** 21414–24